

1 **Statistical Similarities Between WSA-ENLIL+Cone Model and**
2 **MAVEN in situ Observations from November 2014 to March**
3 **2016**

4 **C.L. Lentz¹, D.N. Baker¹, A.N. Jaynes¹, R.M. Dewey², C.O. Lee³, J.S. Halekas⁴, D.A. Brain¹**

5 ¹Laboratory for Atmospheric and Space Physics, University of Colorado, Boulder, CO, USA.

6 ²Department of Climate and Space Sciences and Engineering, University of Michigan, Ann Arbor, MI, USA.

7 ³Space Sciences Laboratory, University of California, Berkeley, CA, USA.

8 ⁴Department of Physics and Astronomy, University of Iowa, Iowa City, Iowa, USA.

9 **Key Points:**

- 10 • Generalized, extensive WSA-ENLIL+Cone model simulations provide analogous confidence
11 levels and results compared to detailed, relatively short simulations.
12 • WSA-ENLIL+Cone model succeeds at predicting fast solar wind radial velocity.

This is the author manuscript accepted for publication and has undergone full peer review but has not been through the copyediting, typesetting, pagination and proofreading process, which may lead to differences between this version and the Version of Record. Please cite this article as doi: [10.1002/2017SW001671](https://doi.org/10.1002/2017SW001671)

Corresponding author: Christy Lentz, christy.lentz@iasp.colorado.edu

Corresponding author: ORCID, orcid.org/0000-0001-6405-0427

Abstract

Normal solar wind flows and intense solar transient events interact directly with the upper Martian atmosphere due to the absence of an intrinsic global planetary magnetic field. Since the launch of the Mars Atmosphere and Volatile Evolution (MAVEN) mission, there are now new means to directly observe solar wind parameters at the planet's orbital location for limited time spans. Due to MAVEN's highly elliptical orbit, in situ measurements cannot be taken while MAVEN is inside Mars' magnetosheath. To model solar wind conditions during these atmospheric and magnetospheric passages, this research project utilized the solar wind forecasting capabilities of the WSA-ENLIL+Cone model. The model was used to simulate solar wind parameters which included magnetic field magnitude, plasma particle density, dynamic pressure, proton temperature, and velocity during a four Carrington rotation-long segment. An additional simulation that lasted 18 Carrington rotations was then conducted. The precision of each simulation was examined for intervals when MAVEN was in the upstream solar wind, i.e., with no exospheric or magnetospheric phenomena altering in situ measurements. It was determined that generalized, extensive simulations have comparable prediction capabilities as shorter, more comprehensive simulations. Generally, this study aimed to quantify the loss of detail in long-term simulations and to determine if extended simulations can provide accurate, continuous upstream solar wind conditions when there is a lack of in situ measurements.

1 Introduction

With the insertion of MAVEN into Mars' orbit on 21 September 2014 (Jakosky et al., 2015), new data coming in are being pored over as MAVEN, among other spacecraft, provides first-hand observations of the long-term effects of solar transient events on Mars' atmosphere. MAVEN has an ~ 4.5 -hour orbit, where it spends at least a few hours in the Magnetosheath, and upwards of approximately two months, when the precessing spacecraft periapsis is at a low solar zenith angle (D. Brain, personal communication, 3 May 2017). Attempting to model solar wind conditions during the MAVEN mission, the WSA-ENLIL+Cone model (Arge & Pizzo, 2000; Odstrčil et al., 2002; Xie et al., 2004) was used for the time period of December 2015 to March 2016, along with a separate run that captured solar wind trends from late November 2014 to March of 2016. We report here on the accuracy of the WSA-ENLIL+Cone model's predictions of solar wind parameters such as the interplanetary magnetic field strength, proton density of the plasma, dynamic pressure, proton temperature and the radial velocity from the two separate runs. We conducted multiple statistical analysis to determine if extended runs are as reliable as relatively short runs. With extensive analysis of the WSA-ENLIL+Cone model's performance, there is a possibility of using the model's predictions for times when MAVEN, or other spacecraft, are unable to obtain in situ measurements during deep-dip campaigns.

Commonly, long term statistical comparisons tend to lose fine detail for individual events. By requesting an extended, lower resolution simulation that overlapped with a portion of a higher-resolution simulation, we could determine what impacts generalizations had on the performance of the model. Expanding on pre-existing performance metrics for solar wind simulations we assessed the model's capacity to provide precise solar wind conditions and to conclude if the extended simulation's results were comparable in accuracy to the detailed run.

2 Background

2.1 The MAVEN Mission

MAVEN is in a highly elliptical orbit with a low altitude periapsis of ~ 150 km, that allows it to pass through the magnetic pileup boundary (MPB) and the bow shock (BS) once every orbit, regardless of the boundary altitudes changes (see Edberg et al., 2009). MAVEN can therefore measure the solar and solar-wind energetic input into the upper atmosphere (e.g., Jakosky et al., 2015), that allows us to explore the interactions of the Sun and the solar wind with the Martian magnetosphere and upper atmosphere. Along with MAVEN there have been multiple other orbiters that can aid in

62 the study of Mars' atmosphere. For example, the Mars Global Surveyor (Acuña et al., 1992) which
63 orbited Mars for ten years, losing signal in November of 2006, had instruments on board such as
64 a Magnetometer (Acuña et al., 1998), but lacked other instruments to observe phenomena such as,
65 Interplanetary Coronal Mass Ejections (ICME) and Solar Energetic Particles (SEP) (Falkenberg et
66 al., 2011). Another recent European mission, the Mars Express (Zender et al., 2009), has atmo-
67 spheric and ionospheric instruments such as the Energetic Neutral Ion analyzer (Barabash et al.,
68 2006), but lacks a magnetometer. For this study, only MAVEN data was used to compare with the
69 WSA-ENLIL+Cone model, however future work in model validation would benefit from having
70 multiple spacecraft data sets to contrast with. MAVEN includes a set of atmosphere-measuring and
71 contextual instruments such as the Solar Wind Electron Analyzer (Mitchell et al., 2016), the Solar
72 Wind Ion Analyzer (Halekas et al., 2015), the Solar Energetic Particle detector (Larson et al., 2015),
73 and a magnetometer (Connerney et al., 2015). However, as MAVEN ascends or descends into the
74 BS and other layering regions, there are time periods when there is no method to extract data on
75 solar wind parameters such as the velocity of the plasma, particle density, pressure, temperature and
76 magnetic field properties. This is where solar wind forecasting models can be utilized to predict
77 supplemental solar wind parameter values (e.g., Dewey et al., 2016).

78 2.2 WSA-ENLIL+Cone Background

79 Among the numerous space weather models that the Community Coordinated Modeling Cen-
80 ter (CCMC) has to offer, the semi-empirical Wang-Sheeley-Arge (Arge & Pizzo, 2000; Arge et
81 al., 2004) solar corona model coupled with the three-dimensional magnetohydrodynamic numeri-
82 cal model, ENLIL (ENLIL v2.8f) (Odstrčil, 2003) combined with the Cone model (Millward et al.,
83 2013; Xie et al., 2004) provide descriptions of the propagation of CMEs to specified orbital loca-
84 tions, such as Mars. This combination of models, along with only WSA-ENLIL, have been used
85 in multiple planetary interaction studies such as at Mercury (e.g., Baker et al., 2009, 2011, 2013;
86 Dewey et al., 2015) or at Earth (e.g., Mays et al., 2015).

87 The WSA model contrives predictions of background solar wind speed and interplanetary mag-
88 netic field (IMF) strength out to $21.5 R_{\odot}$ from maps of the photospheric magnetic field. The WSA
89 model uses the assumption that far from the Sun, the speed of solar wind depends on the path the
90 wind took as it passed through the lower corona. It follows that if the magnetic flux tube, which
91 guided the flow flares out, had large coronal expansion, then the distant speed is slow. Alternatively,
92 if the magnetic flux tube remained focused (i.e., had small coronal expansion) then the distant speed
93 is fast. The extent of expansion is determined from a current-free extension of the photospheric
94 field (Sheeley, 2017). The WSA uses ground-based observations of the solar surface magnetic field
95 as input to a potential-field source surface (PFSS) model (Wang & Sheeley, 1992; Schatten et al.,
96 1969). By applying empirical relationships along with the application of a PFSS magnetic field, the
97 WSA model provides input for ENLIL (Taktakishvili et al., 2009). ENLIL subsequently models the
98 solar wind flow throughout the heliosphere, assuming equal temperatures and densities for electrons
99 and protons with other microscopic processes being neglected (Odstrčil, 2003). The WSA-ENLIL
100 combination then sets the stage for CMEs to be "injected". To include CME disturbances in the
101 WSA-ENLIL model, this study utilized the Cone model. Initially proposed by Zhao et al. (2002)
102 and further refined by Xie et al. (2004), the Cone model is a simplified representation of CME
103 propagation used to characterize 3D geometric and kinematic parameters. The model assumes a
104 constant angular diameter of CMEs in the corona which are enclosed by the external magnetic field.
105 Consequently, Cone-modeled CMEs do not expand in latitude in the lower corona, though they can
106 expand in interplanetary space, as described in Odstrčil et al. (2002).

107 To acquire a WSA-ENLIL+Cone simulation from the CCMC, a list of CME measurements
108 that occurred during the time period of interest must be provided, along with a source for solar
109 magnetograms (e.g., Mount Wilson observatory, Kitt Peak observatory, or Gong observatory). For
110 this study, CME kinematic and geometric properties were gathered from the CCMC Space Weather
111 Database of Notifications, Knowledge, Information (DONKI) database (kawaii.ccmc.gsfc.nasa.gov/DONKI).
112 There, approximated Cone-modeled CME properties derived from coronagraphs were used. The
113 database, which contains a catalog of numerous types of solar activity, is a result of the NASA Space

114 Weather Research Center (SWRC) team daily monitoring of the space environment for NASA's sci-
115 ence campaigns. DONKI continuously updates a list of derived CME geometries that are obtained
116 from spacecraft that are observing a CME event near the solar limb similar to the process described
117 in Lee et al. (2013). It is noted as a limitation of the database that some CMEs may be missed due
118 real-time data gaps (see Mays et al., 2015).

119 The synoptic solar magnetograms chosen for this study were selected from the National Solar
120 Observatory's Global Oscillation Network Group (GONG) (Harvey et al., 1996). GONG's magne-
121 tograms were elected due to their hourly cadence. GONG remaps minute-by-minute images to get a
122 weighted sum to form a full-surface map of the photospheric magnetic flux density (gong.nso.edu).
123 However, it is noted on the model-run request site that GONG data have known issues with the polar
124 fields, which are being studied by the GONG staff (ccmc.gsfc.nasa.gov).

125 It should also be mentioned that the WSA-ENLIL+Cone model's CME arrival times are reliant
126 upon the initial CME geometry input parameters (Mays et al., 2015). Accuracy has also been shown
127 by Lee et al. (2013) to be heavily dependent on the initial precision of the modeled background solar
128 wind, which is determined by the inputted solar magnetograms supplied by the GONG observatories.
129 In comparable studies, the most favorable magnetograms are ones that are updated on an hourly
130 cadence to provide the utmost complete global photosphere magnetic field map.

131 To test the model's validity during the two runs, MAVEN's Solar Wind Ion Analyzer and Mag-
132 netometer were used to determine when MAVEN was in upstream solar wind. The SWIA instru-
133 ment's absolute solar wind density measurements are subject to uncertainties due to ambiguities in
134 the sensitivity calibration as mentioned in Dewey et al. (2016). When comparing MAVEN's proton
135 temperature values to WSA-ENLIL+Cone estimated temperatures, values derived from SWIA for
136 the orbited averaged data are at times overestimated because temperature is a partial moment of the
137 solar wind plasma distribution. This is especially true for the coldest solar wind because due to
138 instrument resolution, the measured distribution will artificially be broadened (J. Halekas, personal
139 communication, 30 March 2017).

140 For both periods of studies, similar to Dewey et al. (2016), we chose SWIA and MAG data
141 from times when MAVEN was considered to be in upstream solar wind. This is characterized by
142 having no exospheric or magnetospheric events present in the data. These observations were then
143 averaged over each orbit, where several filters were applied to the data to determine intervals of
144 upstream solar wind. These filters consisted of altitude, sonic Mach number, the bulk flow velocity,
145 and the root-mean-square (RMS) magnetic field fluctuations. These filters also enabled us to exclude
146 false positives for upstream conditions, for example when MAVEN is taking measurements in Mars'
147 magnetosheath and foreshock.

148 3 Data Observations and Analyses

149 3.1 Analysis of detailed run from December 2015 to March 2016

150 We compared the results from the WSA-ENLIL+Cone model with direct solar wind and IMF
151 measurements from the MAVEN spacecraft over the period from December 2015 to March 2016.
152 In this period of study, there was a total of 83 CMEs documented on the DONKI database, all of
153 which were "injected" into ENLIL. Figure 1 shows the modeled results of the detailed run at the
154 Mars location (black) in comparison with the MAVEN in situ measurements (red).

155 To analyze the accuracy of the detailed WSA-ENLIL+Cone run compared to MAVEN obser-
156 vations, we first identified by how much or how little the modeled distribution underestimates or
157 overestimates each solar wind parameter. To visualize this, Figure 2 includes histograms of the fre-
158 quency distributions of the detailed run from December 2015 to March 2016. The model's data have
159 been orbit-averaged in order to compare to MAVEN's orbit averaged data sets. The bin sizes were
160 chosen specifically for each parameter to adequately represent the data density. Solar wind speed is
161 one of the best represented parameters. These histograms help to demonstrate the performance of
162 the ENLIL component of WSA-ENLIL+Cone. ENLIL is responsible for the output of the five main

163 solar wind parameters examined in this paper after receiving CME parameter information from the
164 WSA and Cone model. The model's strength in capturing solar wind speed distributions can be
165 noted in the last panel of Figure 2. It can also be seen that the mean proton temperature is under
166 predicted for the time period, as was found by Dewey et al. (2016). It is also clear that the WSA-
167 ENLIL+Cone model continuously under predicts IMF strength for CMEs, as stated by Dewey et al.
168 (2015). This can be attributed to the WSA-ENLIL+Cone model not including a magnetic cloud in
169 simulation (see Falkenberg et al., 2011).

170 To compare how well the model does at recovering solar wind transient features, the CME
171 shock arrival times that MAVEN observed are plotted in Figure 3, along with the modeled and
172 in situ wind parameters. These shock arrival times came from the findings of Lee et al. (2017) where
173 MAVEN-observed solar wind transient and energetic particle events were documented. As defined
174 in Falkenberg et al. (2011) a shock at Mars is a jump in the pressure proxy of at least 2 nPa.

175 To evaluate the accuracy of shock detection, we compare the peak dynamic pressure between
176 WSA-ENLIL+Cone and MAVEN. For this time period, the first CME that impacted Mars was on
177 01-02-2016/03:50:00 UT. The peak dynamic pressure value was recorded to be 3.4 nPa. The second
178 CME shock arrival time was recorded to be on 01-06-2016/02:40:00 UT measuring 3.0 nPa. the last
179 impacting CME for this time range was on 02-04-2016/06:05:00 UT and the peak dynamic pressure
180 was recorded at 3.3 nPa.

181 Referencing the WSA-ENLIL+Cone dynamic pressure data set, the model estimated the dy-
182 namic pressure on the 01-02-2016/03:50:00 UT CME to be 0.25 nPa, 01-06-2016/02:40:00 UT at
183 1.59 nPa and finally, 02-04-2016/06:05:00 UT at 0.22 nPa. Therefore, the model underestimated
184 the peak dynamic pressure on average throughout this period by a factor of around 10. It should
185 be noted for this detailed period, that there are many apparent shocks in pressure which are missed
186 by the simulation. The largest shock event, which occurred on 2016-01-13/15:00:00 UT measuring
187 7.59 nPa by MAVEN, was missed by WSA-ENLIL+Cone. The closest event that the model recorded
188 was on 2016-01-14/12:40:00 UT measuring 1.97 nPa.

189 **3.2 Comparison between WSA-ENLIL+Cone model simulation results and MAVEN data** 190 **for an extended time range.**

191 Moving on to the extended simulation, we attempted to determine if this extensive run had an
192 analogous performance to the detailed run. One of the desired insights to gain in this study was to
193 resolve if the extended simulation had loss of detail in any transient disturbances. To determine if the
194 WSA-ENLIL+Cone model could be used to obtain continuous solar wind forcing for an extended
195 period, we requested an extensive simulation from November 2014 to March 2016. The simula-
196 tion of the propagation, evolution, and interaction of solar wind disturbances en route to Mars is a
197 challenging task for such a lengthy stretch of time. The inhomogeneous nature of the flow along
198 with a large spatial domain makes running these simulations computationally expensive. Hence,
199 the extended run had to be broken down into runs. We arbitrarily selected to look at three seasons
200 that composed the simulation for purposes of better visualization. To model the time period from
201 November 2014 to March 2016, the total number of CMEs were filtered. CMEs that were deter-
202 mined to be too slow, or too narrow were excluded from the extended run. For example, CMEs that
203 were detected by the Sun Earth Connection Coronal Heliospheric Investigation (SECCHI) (Howard
204 et al., 2008) on board the Solar Terrestrial Relations Observatory (STEREO A/B) (Kaiser et al.,
205 2007) and Large Angle Spectrometric Coronagraph C2 or C3 on board Solar and Heliospheric Ob-
206 servatory (SOHO) (Domingo et al., 1995) that were detected to be under 300 km/s were excluded
207 along with CMEs that had a half width less than 10. The total number of CMEs documented on the
208 DONKI website for the first winter season of November 2014 to March 2015 was 197; 101 of which
209 were used in the simulation. For the summer season from June 2015 to October 2015, out of the 179
210 total CMEs, 92 were used. Finally, for the second winter period, 46 out of the 83 total CMEs were
211 used. The following figures (Figure 4, 5, and 6) show a broad overview of the data obtained from
212 the WSA-ENLIL+Cone simulation for each of the three seasons.

213 Continuing with preliminary analyses we have included another display (Figure 7) of his-
214 tograms of frequency distributions of the five solar wind parameters from the entire extended period.

215 As was conducted with the detailed simulation, we report on the shock arrival times as observed
216 by MAVEN for the extended run. The shock arrival times for the extended run were also taken from
217 Lee et al. (2017). The second winter period during the extended run is plotted in Figure 8 with
218 identified shock arrival times at MAVEN's orbital location. The values are determined from the
219 orbit-averaged resolution upstream solar wind data set. During the winter period from December
220 2015 to March 2016 for the extended run, MAVEN detected a total of three CMEs. The first arriving
221 on 01-02-16/03:50:00 UT measuring 3.4 nPa, and 01-06-16/02:40:00 UT measuring 3.0 nPa and
222 then on 02-04-16/06:05:00 UT measuring 3.3 nPa. The WSA-ENLIL+Cone model's corresponding
223 dynamic pressure values were 0.16 nPa, 0.16 nPa and 0.87 nPa, respectively. Therefore, on average,
224 the model underestimated peak dynamic pressure by a factor of ~ 15 . Compared to the detailed
225 period where peak dynamic pressure was under predicted by a factor of ~ 10 .

226 The June 2015 to October 2015 season is depicted in Figure 9. MAVEN recorded a CME shock
227 arrival on 07-06-15/20:00:00 measuring 2.1 nPa and a second CME on 10-06-15/17:30:00 measuring
228 3.5 nPa. The WSA-ENLIL+Cone model's corresponding measurements during these time periods
229 were 0.53 and 2.05 nPa respectively. Demonstrating an under-prediction of peak dynamic pressure
230 by a factor of ~ 3 .

231 Figure 10 displays the first winter period from November 2014 to March 2015 where a total of
232 five CMEs made impact with Mars. MAVEN observed the first on 12-18-14/02:00:00 UT measuring
233 1.6 nPa, 02-27-15/02:30:00 UT measuring 4.5 nPa, 03-04-15/04:40:00 measuring 6.5 nPa, 03-07-
234 15/04:00:00 UT measuring 4.5 nPa and finally, 03-08-15/21:00:00 UT measuring 12.5 nPa.

235 The corresponding simulated model values for these time periods were 1.91 nPa at 12-18-
236 2014/02:00:00 UT, 0.69 nPa at 02-27-2015/02:30 UT, 5.97 nPa at 03-04-2015/04:40:00 UT, 1.38
237 nPa at 03-07-2015/04:00:00 UT, and 0.88 nPa at 03-08-2015/21:00:00 UT. The WSA-ENLIL+Cone
238 model therefore under predicted MAVEN observed peak dynamic pressure values by a factor of 5.
239 Averaging the underestimations throughout the entire extended period of analysis, WSA-ENLIL+Cone
240 under predicted observations by a factor of 8. Compared to the detailed period of analysis which
241 under predicted the three documented CMEs by a factor of 10.

242 3.3 Comparison between WSA-ENLIL+Cone model detailed and extended simulation

243 Along with assessing the variability of each data set by examining histograms, we also evalu-
244 ated various moments of both data sets. Measures of skewness and kurtosis were utilized to char-
245 acterize the location and variability of the detailed and extended run. Table 1 and Table 2 display
246 calculated skewness and kurtosis values for the detailed simulation as well as the extended sim-
247 ulation compared to MAVEN. Regarding Table 1, skewness provides information on how outlier
248 events impact the shape of the distribution. Skewness is a measure of symmetry, or the lack thereof.
249 Keeping this in mind, the skewness for a normal distribution is zero. We can therefore look to the
250 calculated values from both MAVEN and the model for the five solar wind parameters to see if
251 the model's skewness is commensurate. For the detailed run all parameters are skewed right as are
252 the MAVEN parameters. Magnetic field magnitude has a right skew (2.25) closest to MAVEN's
253 magnetic field magnitude skew (2.34) suggesting that the run captured the distribution around the
254 mean best out of the other parameters. The first winter period of the extended run was successful
255 in capturing the skewness of MAVEN's recorded B-field magnitude, dynamic pressure, and radial
256 velocity. For the summer season, the model did not capture the skewness of the MAVEN data set as
257 well predominantly in dynamic pressure. For the second winter season, which overlaps in time with
258 the detailed run, the model had an identical skewness score to MAVEN for radial velocity.

259 Table 2 contains the kurtosis values for each parameter. The kurtosis of a data set is defined as
260 the standardized fourth population moment about the mean (Kim, 2013). It is a measure of outlier
261 event impacts on a data set relative to a normal distribution. A higher kurtosis value is produced by
262 infrequent extreme deviations from the mean, as is expected for times of CME impact. The detailed

simulation found a kurtosis of -0.64 for radial velocity, indicating that the distribution produced fewer and less extreme outliers than a normal distribution. This was also true for the extended simulation's first winter and summer season, with kurtosis values of -8.6E-3 and -0.30 respectively. In both simulations, the model exhibits frequent smaller deviations from the mean as is evident by the smaller valued kurtosis measurements relative to MAVEN's.

To measure prediction accuracy of the two models, we also calculated the mean square error (MSE). Averaging the three season's MSEs during the extended time period, it was found that the average MSE for IMF strength was 11.79 nT² and 10.11 nT² for the detailed run. The proton density (N) had a MSE of 11.50 cm⁻⁶ for the extended and 8.70 cm⁻⁶ for the detailed. The dynamic pressure (P) was 0.74 nPa² for the extended; 0.72 nPa² for the detailed. Proton temperature (T) MSE was calculated to be 50.79 eV² for the extended; 44.83 eV² for the detailed run. Finally, radial solar wind velocity (V) MSE was found to be 1.3E4 km²/s² for the extended run compared to 1.21E4 km²/s² for the detailed. These results are summarized in Table 3. Note that a value closer to zero displays better agreement between the two data sets.

Continuing with the parameter comparisons in Table 4, we found the ratio of median values modeled by WSA-ENLIL+Cone and observed by various MAVEN instruments for the detailed run and for the extended run. Ratios of medians were evaluated because medians have robustness of validity, meaning they are not greatly affected by outliers. Here values closer to one display excellent agreement between the model and the observations. We see that the averaged median ratio of the IMF strength estimated by WSA-ENLIL+Cone compared to MAVEN (B_{WEC}/B_{MAVEN}) for the extended run is 0.59 compared to the detailed run which was 0.39. Averaged (N_{WEC}/N_{MAVEN}) for the extended run was 0.63 and 0.56 for the detailed. Averaged (P_{WEC}/P_{MAVEN}) was 0.75 for the extended period compared to 0.54 for the detailed period. (T_{WEC}/T_{MAVEN}) for the extended time period was 0.44 compared to 0.31 for the detailed period. (V_{WEC}/V_{MAVEN}) was 1.09 for the extended period and 1.01 for the detailed period.

To conduct an all-encompassing comparison of means, we then calculated the two-sample t-test as described in Snedecor and Cochran (1996). Briefly stating the importance of the t-test; the computation calculates the difference between the observed means in two independent data sets. The summary statistics returned from the test include the difference of the means, the standard error between the means, a 95% Confidence Interval (CI), the t-statistic, and a significance value commonly referred to as the P-value. The P-value is defined as the probability of obtaining the observed differences between data sets if the difference between the two means was zero (otherwise known as the null hypothesis). If the P-value is low ($P < 0.05$) the variances of the two samples cannot be assumed to be equal. The t-statistic measures the size of the difference relative to the variation of the data sets. Larger t-statistics represent evidence that there is significant difference from the two datasets. Table 5 lists the summary of statistics. It was found that for the detailed simulation, the only solar wind parameter that was above the conventional 0.05 P-value was that of the radial velocities, reaching a P-value of 0.16. The extended simulation did not reach P-values higher than 0.0001, causing the null hypothesis to be rejected. We therefore conclude that the WSA-ENLIL+Cone model's and MAVEN's means for each of the five solar wind parameters differed considerably.

Delving a little deeper into calculating t-test statistics, and taking into consideration that solar wind exists in two fundamental states of slow and fast, we sorted each data set into corresponding fast and slow solar wind. Based off of Schwenn (2001) definitions of average solar wind parameters for times around solar minimum, we classified slow solar wind as having an average radial velocity between 250 - 400 km/s, a proton density of $\sim 10.7 \text{ cm}^{-3}$ and proton temperature of $\sim 3 \text{ eV}$. Fast solar wind, on the other hand, was classified as having an average velocity between 400 - 800 km/s, an average proton density of $\sim 3 \text{ cm}^{-3}$, and proton temperature averaging $\sim 19.82 \text{ eV}$. Based on these definitions of fast and slow solar wind, once more we calculated the two-sample t-test for the unpaired data sets. For the sake of brevity, we have only included the absolute value of the t-statistic and the significance level (P-value). Table 6 includes the t-statistic and its P-value for proton density, proton temperature, and radial velocity for fast and slow solar wind. While categorizing slow and fast solar wind, there were instances where the WSA-ENLIL+Cone model's orbit-averaged data did

316 not include any values matching Schwenn (2001) averages. These are identified in Table 6 as dash
317 marks. It was found that for the detailed run, fast solar wind radial velocity had the highest P-value,
318 reaching 0.40. For the extended run, fast solar wind radial velocity again had the highest P-values.
319 These P-values, in chronological order, were 0.58, 0.20 and 0.27. For the summer season of the
320 extended run, the slow solar wind velocity had a P-value of 0.16, exhibiting statistical significance.

321 **4 Discussion and Conclusion**

322 The data provided by spacecraft orbiting Mars allows model developers to regularly adjust
323 solar wind and interplanetary magnetic field modeling for reliability and overall validity. It has been
324 shown in multiple studies (e.g., Dewey et al., 2015, 2016; Lee et al., 2015) that even in detailed
325 runs, the WSA-ENLIL+Cone model does not completely capture trends of observed solar wind and
326 IMF properties (e.g., under-prediction of IMF strength, systematic over prediction of temperature).
327 There is still much work to be done, such as using in situ observations from multiple spacecraft to
328 cross-check model outcomes.

329 Regarding the inaccuracies of amplitudes and arrival times of CME shocks, we can turn to the
330 mathematical description of ENLIL to see what postulations are made. In Odstrčil (2003) a magne-
331 tohydrodynamic (MHD) approximation was used. Included in the approximation are equations for
332 total mass density, mean flow velocity, magnetic field, total pressure, and thermal energy. It is noted
333 that in this MHD approximation, thermal energy is used instead of total energy to produce smooth
334 profiles for the thermal pressure and temperature. With the use of this thermal energy equation, it is
335 recognized that it may lead to inaccuracies in speed and amplitude of strong shocks. The discrepan-
336 cies in CME arrival times can also be attributed to the inverse correlation between solar wind speed
337 and density (see Lee et al., 2013). The spherical plasma clouds used in simulation are initialized
338 to have uniform velocities along with temperatures being set equal to that of the ambient fast solar
339 winds. The ratio of the CME cloud density to the ambient fast solar wind density is not discernible
340 from observations, therefore the plasma cloud, by default, has a larger dynamic pressure value than
341 the pressure of the ambient fast wind. This results in the modeled CME being injected into a denser
342 solar wind stream that is moving at relatively slow speeds. This causes the CME shock arrival time
343 to be later than observed, as proven by Taktakishvili et al. (2010).

344 High speed stream arrival times can be impacted by WSA coronal maps that contain small
345 latitudinal shifts in the magnetogram-derived coronal maps. These shifts, as pointed out in Mays et
346 al. (2015), can be caused by inaccuracies in solar magnetic-field observations subsequently causing
347 large longitudinal shifts in the solar wind structure. With improvements to global photospheric
348 maps using magnetic flux transport models or the implementation of inter-calibrated magnetograms
349 from multiple sources, we would be able to predict the magnetic field in locations where direct
350 measurements are not available or possible. This would in turn improve background solar wind
351 modeling, subsequently improving CME event densities.

352 Turning to the Cone model, there exists variations in cone parameters generated for each CME
353 event. Due to the fact that the cone model relies on manual fits of an ellipse over a white light
354 coronagraph of a CME, ambiguities in identifying the ejecta structure lead to discord in 3D CME
355 kinematic and geometric parameter estimations. Furthermore, there are known assumptions of CME
356 properties such as isotropic expansion of CMEs, radial propagation, and constant CME cone angu-
357 lar width. Also due to temporal and spatial resolution limitations, the model is constructed to only
358 reproduce large-scale magnetic configurations. This translates to the model not incorporating mag-
359 netic fields within ejecta such as a flux ropes. As found by Falkenberg et al. (2011), many ICMEs
360 change direction in propagation so assuming radial propagation from their point of origin may not be
361 valid in all cases. Zhao et al. (2002) in turn concludes that numerous CMEs propagate almost radi-
362 ally, signifying that their angular widths remain nearly constant throughout the corona and therefore
363 provide a basis for propagation.

364 Both the extended and detailed runs discrepancies with in situ observations are inherently linked
365 to these various assumptions in each model. It can be asserted that the WSA-ENLIL+Cone model

366 could one day provide a point of reference for solar wind parameters such as radial velocity for
367 extensive and/or short time periods. We have shown this through collating multiple statistics such
368 as skewness and kurtosis measurements, the two-sample t-tests for five important solar wind param-
369 eters, comparison of fast and slow solar wind data, MSE values, and ratios of medians. Conducting
370 systematic validation of the model in both solar minima and maxima can highlight the underlying
371 problems experienced when forecasting solar wind parameters to planetary orbital locations. This
372 study was an effort to contribute to the model's development and to establish that generalized simu-
373 lations, which include less solar transient events, perform the same as comprehensive runs.

374 We, therefore, conclude that with current day restrictions of computational-grid resolutions
375 among other things, the long-term simulations demonstrate no loss of detail compared to shorter,
376 exhaustive simulations. Generally, solar wind modeling should be used in conjunction with other
377 techniques such as solar wind proxies to provide more thorough characterizations of solar wind
378 conditions at Mars. As low computational overhead becomes less of a worry, each new refinement
379 of the model will be expected to render more realistic computations. In this case, long-term forecasts
380 might continue to have imprecise predictions, however, the short all-inclusive forecasts will be closer
381 to what is actually observed in nature.

382 **Acknowledgments**

383 The MAVEN project is supported by NASA through the Mars Exploration Program. All original
384 MAVEN data reported in this paper is archived by the NASA Planetary Data System (<https://pds.nasa.gov/>)
385 and is available for public use. C. L. Lentz thanks M. L. Mays for providing valuable input
386 on the models and who also conducted all of the simulations. The modeling techniques described
387 in this paper were originally developed under the auspices of the National Science Foundation's
388 Center for Integrated Space Weather Modeling (CISM). Simulation results have been provided by
389 the Community Coordinated Modeling Center at the Goddard Space Flight Center through their
390 public Runs on Request system (ccmc.gsfc.nasa.gov; run numbers: Christy_Lentz.081216_SH.1,
391 Christy_Lentz.081216_SH.2, Christy_Lentz.081216_SH.3, Christy_Lentz.081216_SH.4, Christy_Lentz.081216_SH.5,
392 and Christy_Lentz.01102017.SH.1). The WSA model was developed by N. Arge (NASA GSFC)
393 and the ENLIL Model was developed by D. Odstrčil (GMU).

394 **5 References**

- 395 Acuña, M. H., Connerney, J. E. P., Wasilewski, P., Lin, R. P., Anderson, K. A., Carlson, C. W., ...
396 Ness, N. F. (1992), Mars Observer Magnetic Fields Investigation. *Journal of Geophysical Research*,
397 97(E5), 7799-7814. doi:10.1029/92JE00344
- 398 Acuña, M. H., Connerney, J. E. P., Wasilewski, P., Lin, R. P., Anderson, K. A., Carlson, C. W., ...
399 Ness, N. F. (1998), Magnetic Field and Plasma Observations at Mars: Initial Results of the Mars
400 Global Surveyor Mission. *Science*, 279(5357), 1676-1680. doi:10.1126/science.279.5357.1676
- 401 Arge, C. N., & Pizzo, V. J. (2000), Improvement in the Prediction of Solar Wind Conditions Using
402 Near-Real Time Solar Magnetic Field Updates. *Journal of Geophysical Research: Space Physics*,
403 105(A5), 10465-10479. doi:10.1029/1999JA000262
- 404 Arge, C. N., Luhmann, J. G., Odstrčil, D., Schrijver, C. J., & Li, Y. (2004), Stream structure and
405 Coronal Sources of the Solar Wind during the May 12th, 1997 CME. *Journal of Atmospheric and*
406 *Solar-Terrestrial Physics*, 66, 1295-1309. doi:10.1016/j.jastp.2004.03.018
- 407 Baker, D. N., Odstrčil, D., Anderson, B. J., Arge, C. N., Benna, M., Gloeckler, G., ... Zurbuchen,
408 T. H. (2009), Space Environment of Mercury at the Time of the First MESSENGER Flyby: Solar
409 Wind and Interplanetary Magnetic Field Modeling of Upstream Conditions. *Journal of Geophysical*
410 *Research: Space Physics*, 114, A10101. doi:10.1029/2009JA014287

- 411 Baker, D. N., Odstrčil, D., Anderson, B. J., Arge, C. N., Benna, M., Gloeckler, G., ... Zurbuchen, T.
412 H. (2011), The Space Environment of Mercury at the Times of the Second and Third MESSENGER
413 Flybys. *Planetary and Space Science*, 59(15), 2066-2074. doi: 10.1016/j.pss.2011.01.018.
- 414 Baker, D. N., Poh, G., Odstrčil, D., Arge, C. N., Benna, M., Johnson, C. L., ... Zurbuchen, T.
415 H. (2013), Solar Wind Forcing at Mercury: WSA-ENLIL Model Results. *Journal of Geophysical
416 Research: Space Physics*, 118.1: 45-57. doi:10.1029/2012JA018064
- 417 Barabash, S., Lundin, R., Andersson, H., Brinkfeldt, K., Grigoriev, A., Gunell, H., ... Wurz, P.
418 (2006). The Analyzer of Space Plasmas and Energetic Atoms (ASPERA-3) for the Mars Express
419 Mission. *Space Science Reviews* 126, 113-164. doi:10.1007/s11214-006-9124-8
- 420 Connerney, J. E. P., Espley, J., Lawton, P., Murphy, S., Odom, J., Oliverson, R., & Sheppard, D.
421 (2015), The MAVEN Magnetic Field Investigation. *Space Science Reviews*, 195:257, doi:10.1007/s11214-
422 015-0169-4
- 423 Dewey, R. M., Baker, D. N., Anderson, B. J., Benna, M., Johnson, C. L., Korth, H., ... Odstrčil,
424 D. (2015), Improving Solar Wind Modeling at Mercury: Incorporating Transient Solar Phenomena
425 into the WSA-ENLIL Model with the CONE Extension. *Journal of Geophysical Research: Space
426 Physics*, 120:7, 5667-5685. doi:10.1002/2015JA021194
- 427 Dewey, R. M., Baker, D. N., Mays, M. L., Brain, D. A., Jakosky, B. M., Halekas, J. S., ... Lee, C.
428 O. (2016), Continuous Solar Wind Forcing Knowledge: Providing Continuous Conditions at Mars
429 with the WSA-ENLIL+Cone Model. *Journal of Geophysical Research: Space Physics*, 121.7 :
430 6207-6222. doi:10.1002/2015JA021941
- 431 Domingo, V., Fleck, B., & Poland, A. I. (1995), SOHO: The Solar and Heliospheric Observatory.
432 *Space Science Reviews*, 72.1-2: 81-84. doi:10.1007/BF00768758
- 433 Edberg, N. J. T., Brain, D. A., Lester, M., Cowley, S. W. H., Modolo, R., Fränz, M., & Barabash,
434 S. (2009), Plasma Boundary Variability at Mars as Observed by Mars Global Surveyor and Mars
435 Express. *Annales Geophysicae*, 27.9: 3537-550. doi:10.5194/angeo-27-3537-2009
- 436 Falkenberg, T. V., Taktakishvili, A., Pulkkinen, A., Vennerstrom, S., Odstrčil, D., Brain, D. A., ...
437 Mitchell, D. (2011), Evaluating Predictions of ICME Arrival at Earth and Mars, *Space Weather*, 9,
438 S00E12. doi:10.1029/2011SW000682
- 439 Halekas, J. S., Taylor, E. R., Dalton, G., Johnson, G., Curtis, D. W., McFadden, J. P., ... Jakosky,
440 B. M. (2015), The Solar Wind Ion Analyzer for MAVEN, *Space Science Reviews*, 195, 125-151.
441 doi:10.1007/s11214-013-0029-z
- 442 Harvey, J. W., Hill, F., Hubbard, R. P., Kennedy, J. R., Leibacher, J. W., Pintar, J. A., ... Yasukawa,
443 E. (1996), The Global Oscillation Network Group (GONG) Project. *Science*, 272, 5266, 1284-1286.
444 doi:10.1126/science.272.5266.1284
- 445 Howard, R. A., Moses, J. D., Vourlidas, A., Newmark, J. S., Socker, D. G., Plunkett, S. P., ... Carter,
446 T. (2008), Sun Earth Connection Coronal and Heliospheric Investigation (SECCHI). *Space Science
447 Reviews*, 136.1-4, 67-115. doi:10.1007/s11214-008-9341-4
- 448 Jakosky, B. M., Grebowsky, J. M., Luhmann, J. G., Connerney, J. E. P., Eparvier, F., Ergun, R., ...
449 Yelle, R. (2015), MAVEN Observations of the Response of Mars to an Interplanetary Coronal Mass
450 Ejection. *Science*, 350(6261). doi:10.1126/science.aad0210
- 451 Kaiser, M. L., Kucera, T. A., Davila, J. M., St. Cyr, O. C., Guhathakurta, M., & Christian, E. (2007),
452 The STEREO Mission: An Introduction. *Space Science Reviews*, 136.1-4, 5-16. doi:10.1007/s11214-
453 007-9277-0
- 454 Kim, H. Y. (2013), Statistical Notes for Clinical Researchers: Assessing Normal Distribution (2) us-
455 ing Skewness and Kurtosis. *Restorative Dentistry and Endodontics*, 38(1), 52-54. [https://doi.org/10.5395/
456 rde.2013.38.1.52](https://doi.org/10.5395/rde.2013.38.1.52)

- 457 Larson, D. E., Lillis, R. J., Lee, C. O., Dunn, P. A., Hatch, K., Robinson, M., ... Jakosky, B.M.
458 (2015), The MAVEN Solar Energetic Particle Investigation. *Space Science Reviews*, 195.1-4, 153-
459 172. doi:10.1007/s11214-015-0218-z
- 460 Lee, C. O., Arge, C. N., Odstrčil, D., Millward, G., Pizzo, V., Quinn, J. M., & Henney, C. J. (2013),
461 Ensemble Modeling of CME Propagation. *Solar Physics*, 285.1-2, 349-368. doi:10.1007/s11207-
462 012-9980-1
- 463 Lee, C. O., Arge, C. N., Odstrčil, D., Millward, G., Pizzo, V., & Lugaz, N. (2015), Ensemble Model-
464 ing of Successive Halo CMEs: A Case study, *Solar Physics*, 290, 1207-1229. doi:10.1007/s11207-
465 015-0667-2
- 466 Lee, C. O., Hara, T., Halekas, J. S., Thiemann, E., Chamberlin, P., Eparvier, F., ... Jakosky, B. M.
467 (2017), MAVEN Observations of the Solar Cycle 24 Space Weather Conditions at Mars. *Journal of*
468 *Geophysical Research: Space Physics*, 122, 2768-2794. doi:10.1002/2016JA023495
- 469 Mays, M. L., Taktakishvili, A., Pulkkinen, A., MacNeice, P. J., Rastätter, L., Odstrčil, D., ...
470 Kuznetsova, M. M. (2015), Ensemble Modeling of CMEs Using the WSA-ENLIL Cone Model. *Solar*
471 *Physics*, 290.6, 1775-1814. doi:10.1007/s11207-015-0692-1
- 472 Millward, G., Biesecker, D., Pizzo, V., & De Koning, C. A. (2013), An Operational Software Tool
473 for the Analysis of Coronagraph Images: Determining CME Parameters for Input into the WSA-
474 ENLIL Heliospheric Model. *Space Weather*, 11.2, 57-68. doi:10.1002/swe.20024
- 475 Mitchell, D.L., Mazelle, C., Sauvaud, J.A., Thocaven, J., Rouzaud, J., Fedorov, A., ... Jakosky,
476 B.M. (2016), The MAVEN Solar Wind Electron Analyzer. *Space Science Reviews*, 200, 495-528.
477 <https://doi.org/10.1007/s11214-015-0232-1>
- 478 Odstrčil, D. (2003), Modeling 3-D Solar Wind Structure. *Advances in Space Research*, 32.4, 497-
479 506. doi:10.1016/S0273-1177(03)00332-6
- 480 Odstrčil, D., Linker, J. A., Lionello, R., Mikic, Z., Riley, P., Pizzo, V. J., & Luhmann, J. G. (2002),
481 Merging of Coronal and Heliospheric Numerical Two-Dimensional MHD Models. *Journal of Geo-*
482 *physical Research: Space Physics*, 107(A12), 1493. doi:10.1029/2002JA009334
- 483 Schatten, K.H., Wilcox, J.M. & Ness, N.F. (1969), A Model of Interplanetary and Coronal Magnetic
484 Fields. *Solar Physics*, 6, 442-455. <https://doi.org/10.1007/BF00146478>
- 485 Schwenn, R. (2001), Solar Wind: Global Properties. *Encyclopedia of Astronomy and Astrophysics*,
486 doi:10.1888/0333750888/2301
- 487 Sheeley Jr., N. R. (2017), Origin of the Wang-Sheeley-Arge Solar Wind Model. *History of Geo-*
488 *physics and Space Sciences*, doi:10.5194/hgss-8-21-2017
- 489 Snedecor, G. W., & Cochran, W. G. (1996), *Statistical Methods*. (Vol. 8). Ames, IA: Iowa State
490 University Press.
- 491 Taktakishvili, A., Kuznetsova, M., MacNeice, P., Hesse, M., Rastätter, L., Pulkkinen, A., ... Odstrčil,
492 D. (2009), Validation of the Coronal Mass Ejection Predictions at the Earth Orbit Estimated by
493 ENLIL Heliosphere Cone Model. *Space Weather*, 7, doi:10.1029/2008SW000448
- 494 Taktakishvili, A., MacNeice, P., & Odstrčil, D. (2010), Model Uncertainties in Predictions of Arrival
495 of Coronal Mass Ejections at Earth Orbit, *Space Weather*, 8, S06007. doi:10.1029/2009SW000543
- 496 Wang, Y. M., & Sheeley, N. R. (1992), On Potential Field Models of the Solar Corona. *Astrophysical*
497 *Journal*, 392, 310-319. doi:10.1086/171430
- 498 Xie, H., Ofman, L. & Lawrence, G. (2004), Cone Model for Halo CMEs: Application to Space
499 Weather Forecasting. *Journal of Geophysical Research*, 109, A3. doi:10.1029/2003JA010226

500 Zender, J., Delhaise, F., Arviset, C., Heather, D., Diaz Del Rio, J., Manaud, N., ... & Slavney, S.
501 (2009), Mars Express: The Scientific Investigations, 257-278, Noordwijk, the Netherlands: ESA
502 Special Publication SP-1291.

503 Zhao, X. P., Plunkett, S. P., & Liu, W. (2002), Determination of Geometrical and Kinematical Prop-
504 erties of Halo Coronal Mass Ejections using the Cone Model *Journal of Geophysical Research*, 107,
505 A8, doi:10.1029/2001JA009143

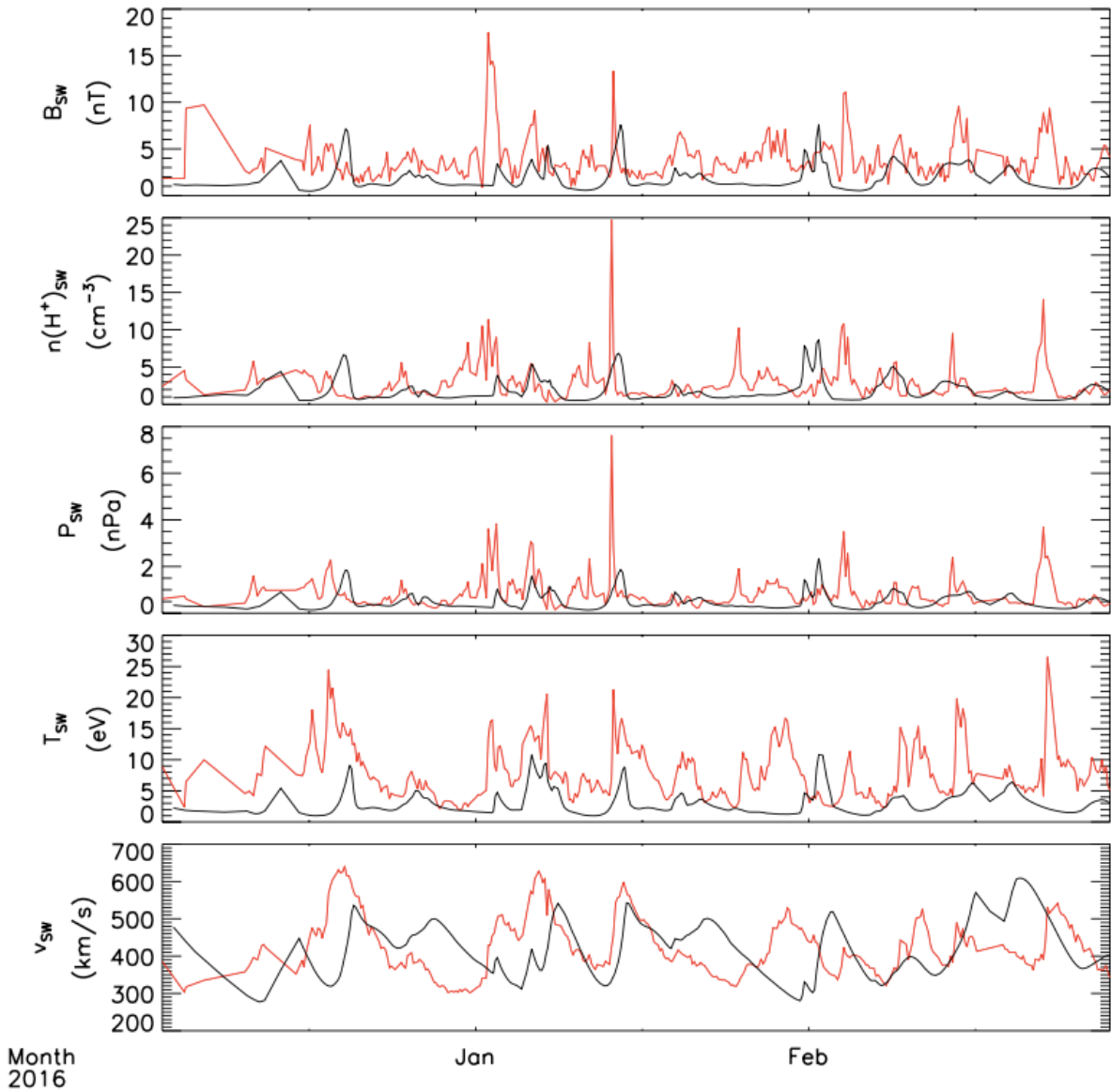


Figure 1: The WEC model results for the detailed period from December 2015 to March 2016. WEC (black) computed values and MAVEN (red) actual observations of IMF B, and solar wind parameters N, P, T and V are shown from the first to the fifth panel, respectively. Note the sparsity of MAVEN’s data at the beginning of this time period is due to MAVEN not being in an interval of pristine solar wind

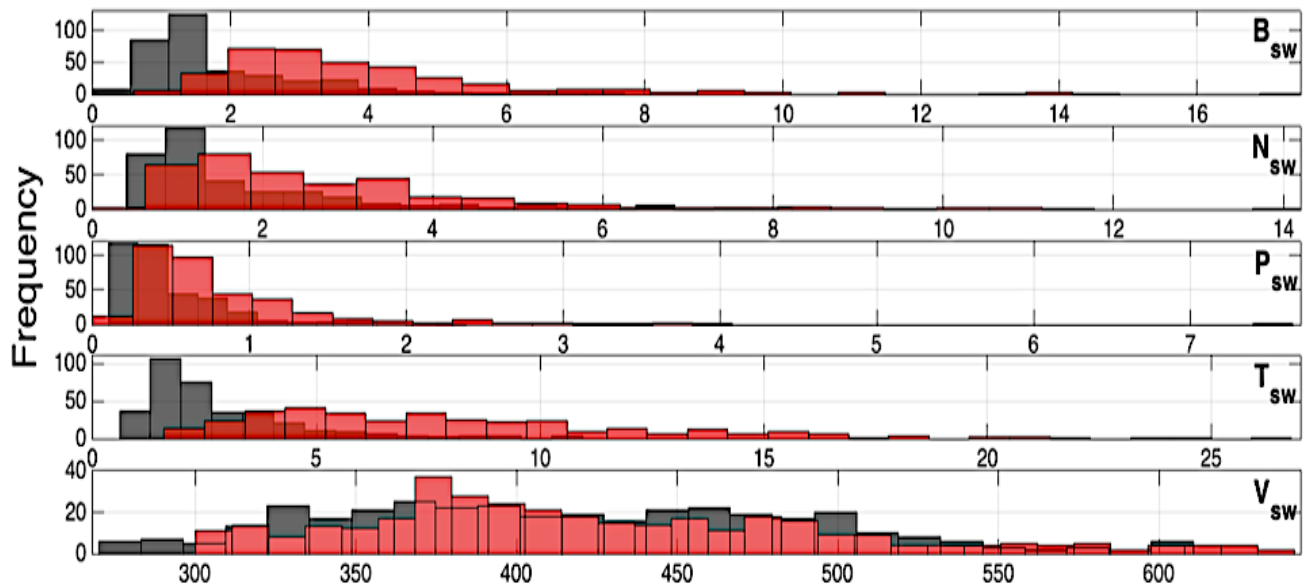


Figure 2: Histograms of frequency distributions from the entire detailed run from December 2015 to March 2016. The model's data (black) have been orbit-averaged to compare to MAVEN's orbit-averaged data sets (red). The bin sizes were chosen specifically for each parameter to adequately represent the data density



Figure 3: Identified CME shock arrival times depicted in light green from the detailed simulation (December 2015 to March 2016). MAVEN's observations are depicted in red, while WSA-ENLIL+Cone dataset is in black.

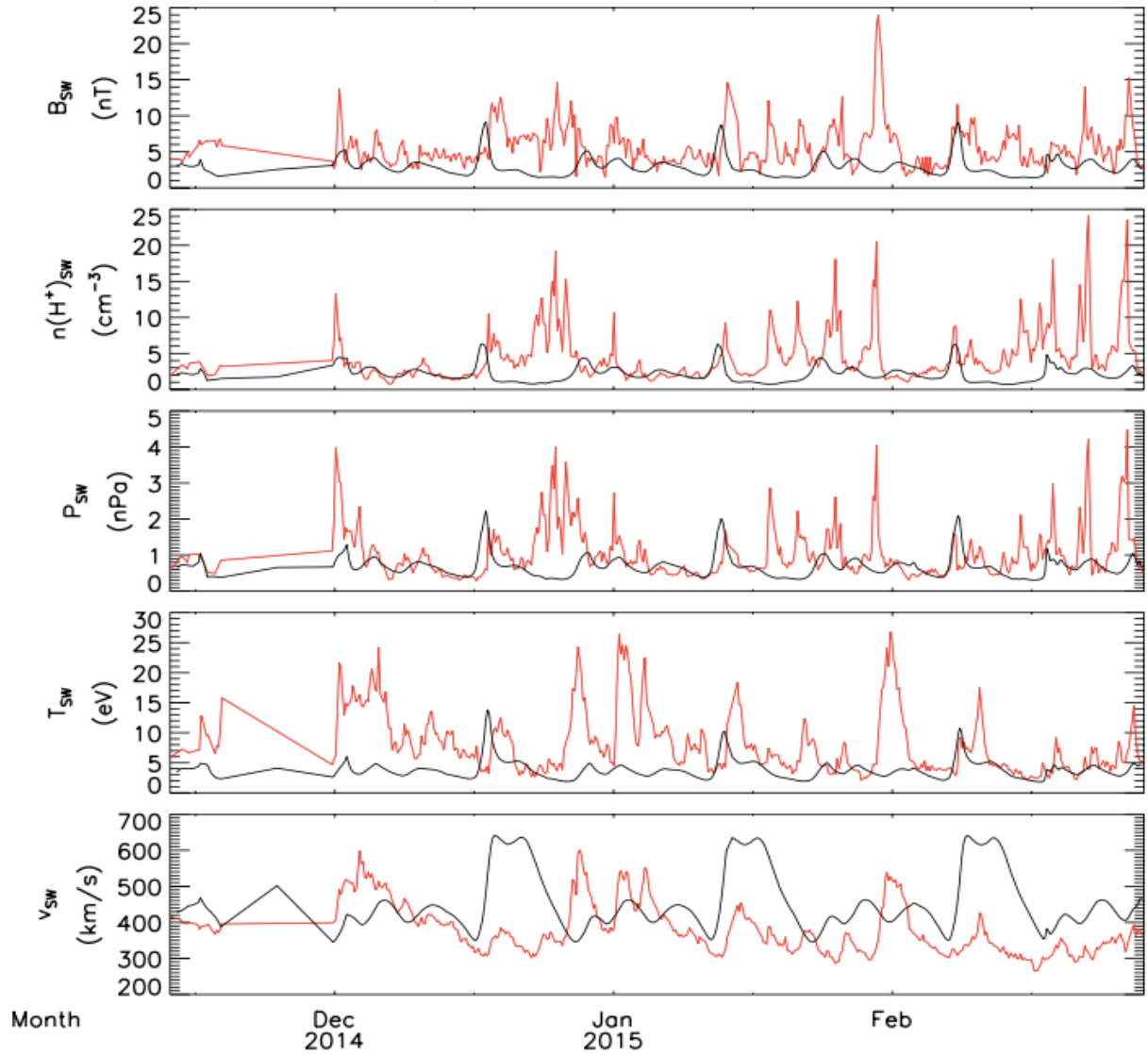


Figure 4: The WEC model results (black) for the extended run from November 2014 to March 2015, along with MAVEN observations (red). The five solar wind parameters in each panel are as follows: magnitude of the IMF (B) measured in nT, the number of protons in solar wind (N) measured in cm^{-3} , the dynamic pressure (P) measured in nPa, the magnitude of temperature (T) measured in eV, and radial velocity measured in km/s

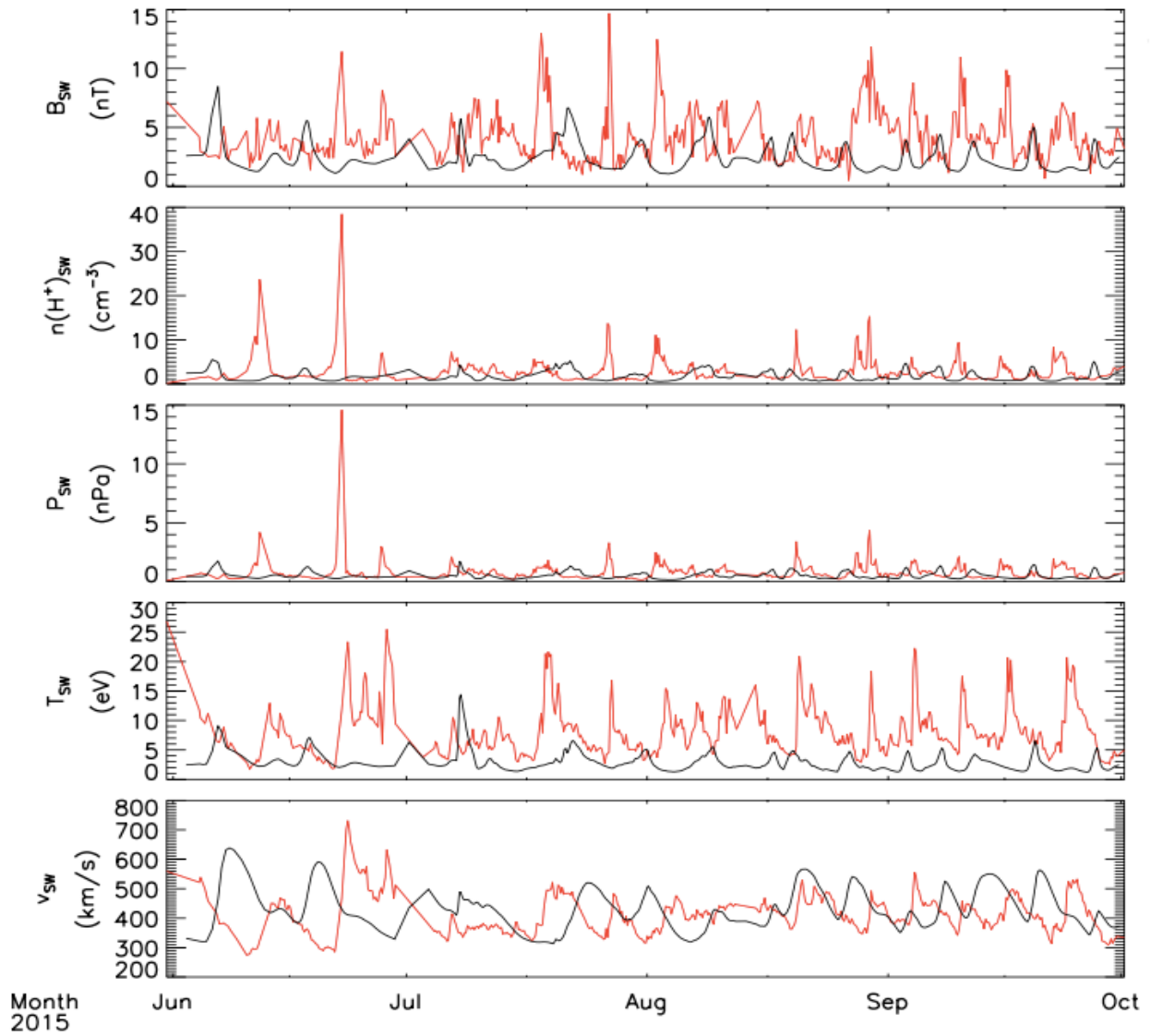


Figure 5: The WEC model results (black) for the extended run from June 2015 to October 2015 along with MAVEN observations (red)

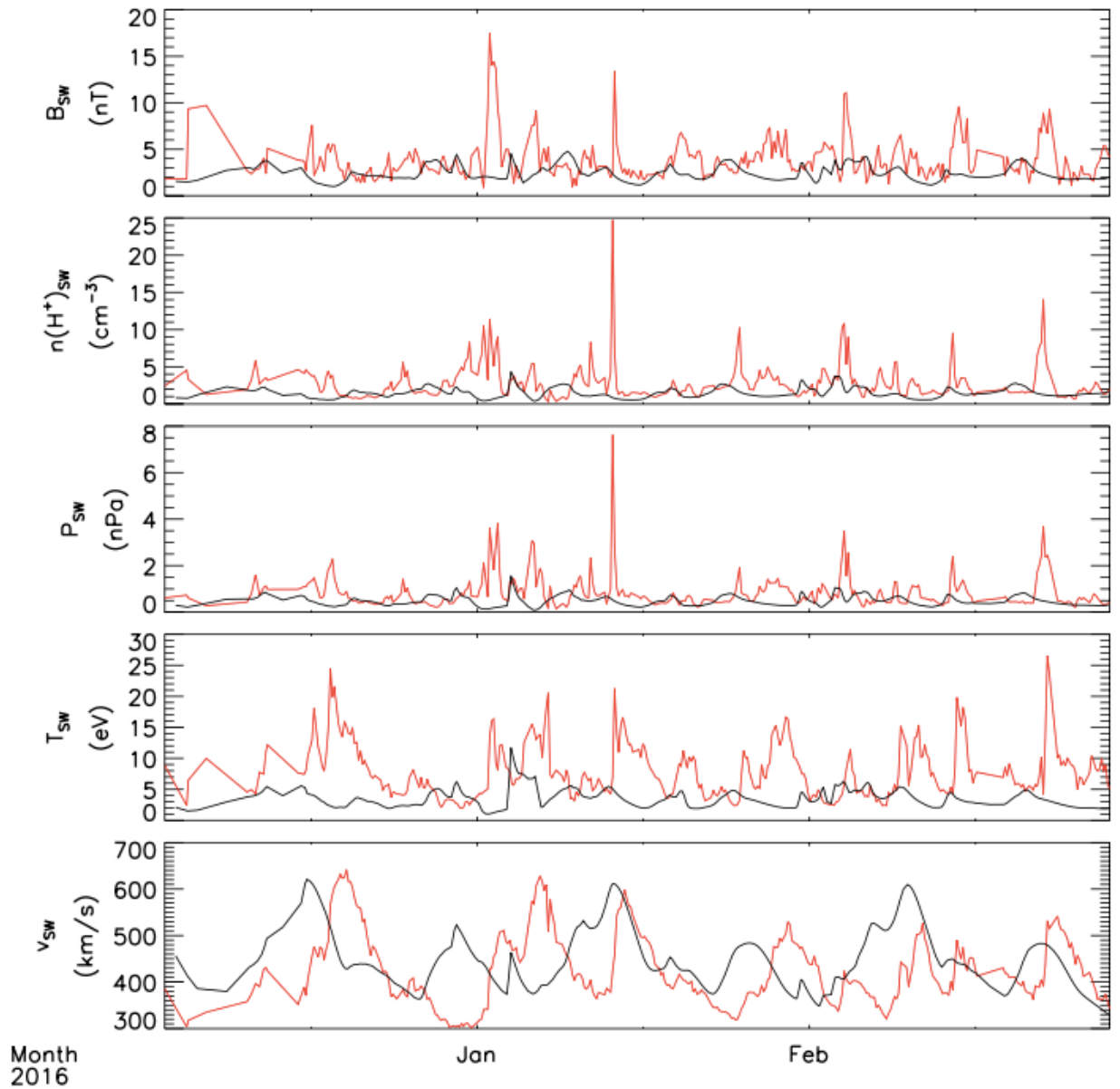


Figure 6: The WEC model results (black) for the extended run from December 2015 to March 2016. December 2015 to March 2016 season plotted for extended run, along with MAVEN observations (red)

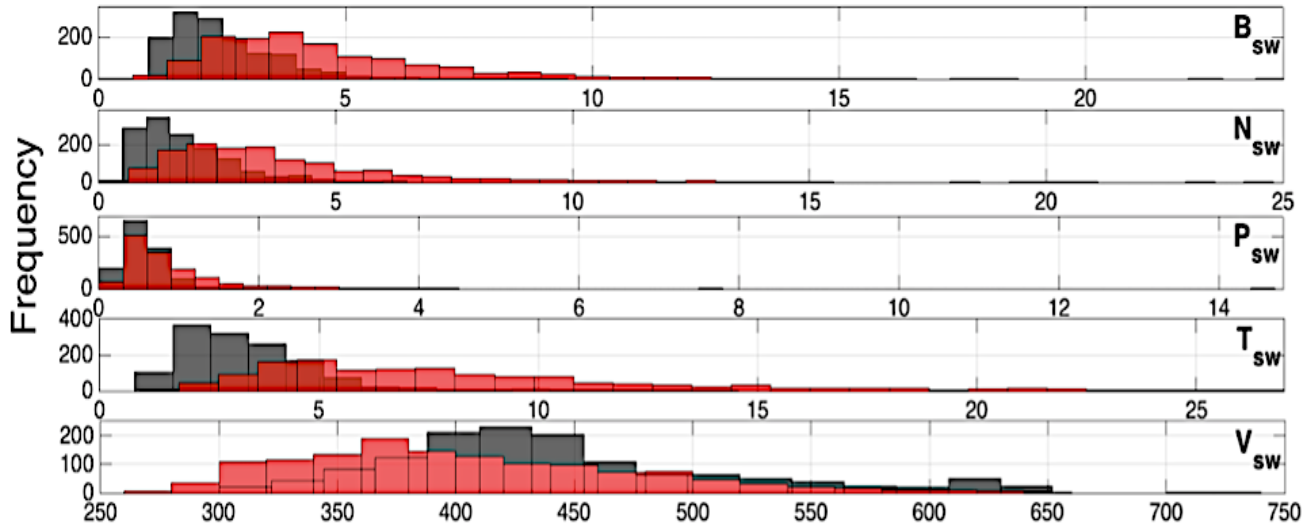


Figure 7: Histograms of frequency distributions from the entire extended run from November 2014 to March 2016. Where the model's data (black) have been orbit-averaged to compare to MAVEN's orbit-averaged data sets (red). The bin sizes were chosen specifically for each parameter to adequately represent the data density.

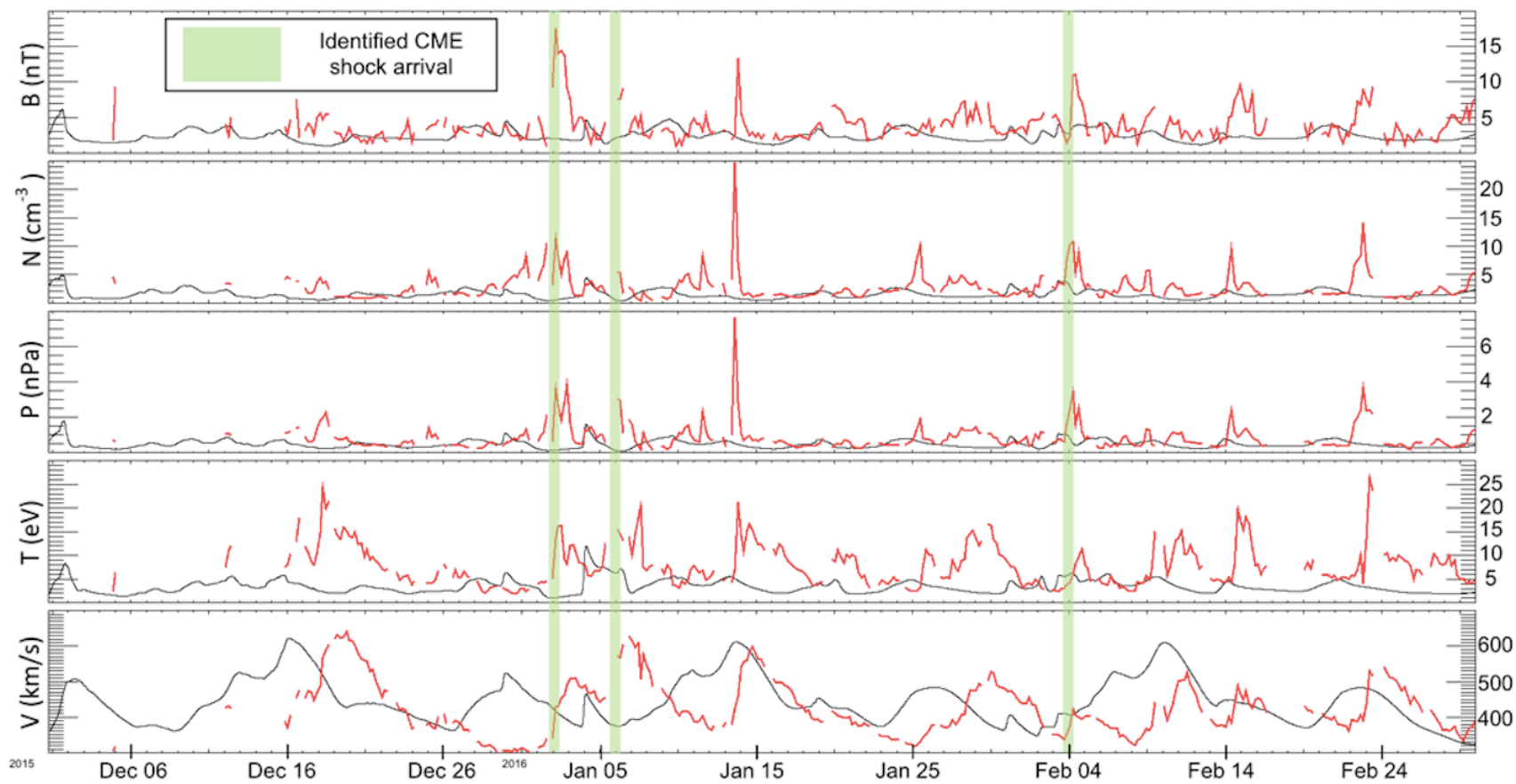


Figure 8: Identified CME shock arrival times (light green) from December 2015 to March 2016 for the extended run as observed by MAVEN (red) and predicted by WSA-ENLIL+Cone (black)



Figure 9: Identified CME shock arrival times (light green) from June to October 2015 for the extended run as observed by MAVEN (red) and predicted by WSA-ENLIL+Cone (black)

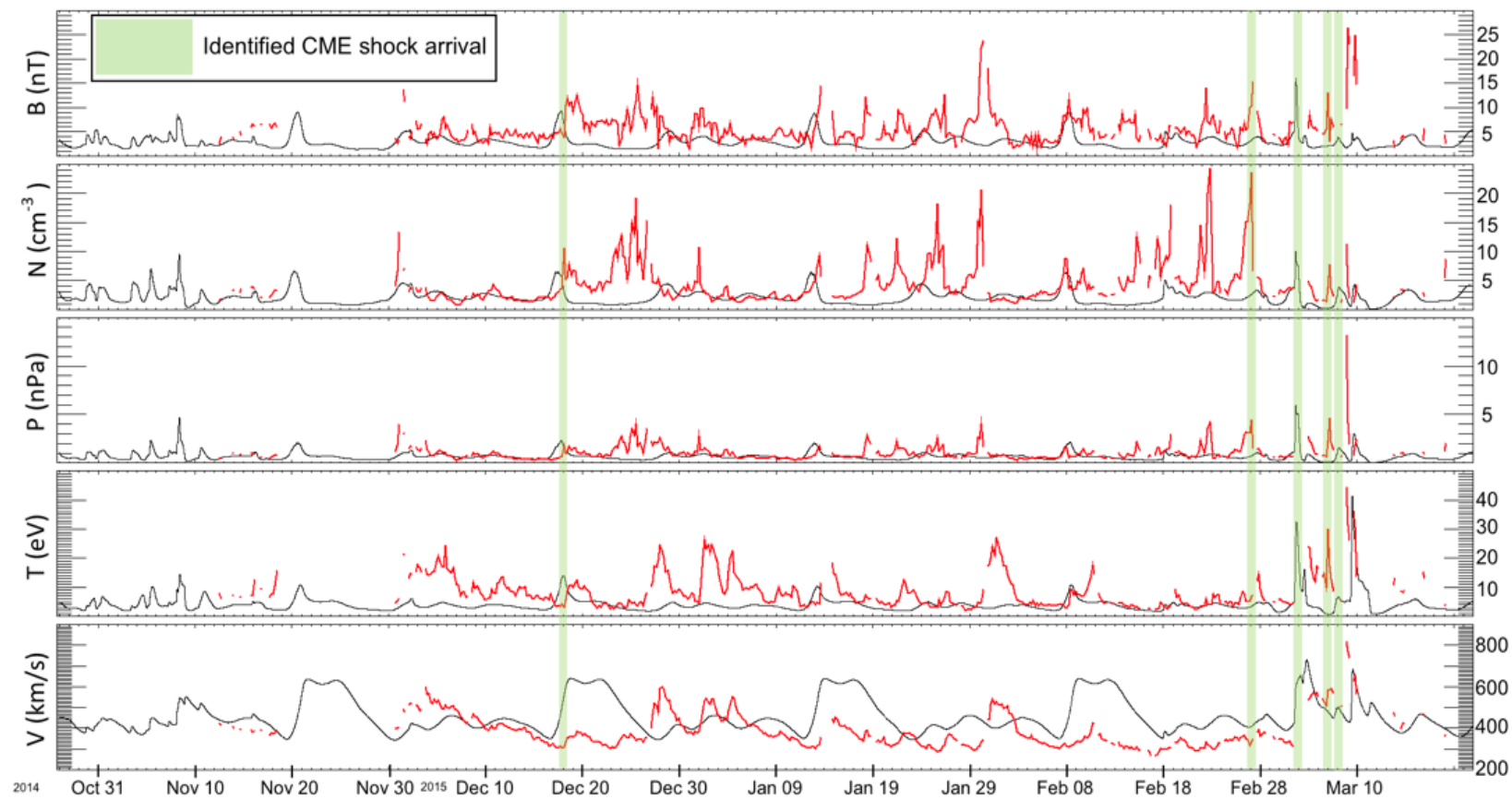


Figure 10: Identified CME shock arrival times (light green) from November 2014 to March 2015 for the extended run as observed by MAVEN (red) and predicted by WSA-ENLIL+Cone (black)